Supporting Information: Electron–phonon-driven three-dimensional metallicity in an insulating cuprate

Edoardo Baldini[a,b,1], **Michael A. Sentef**[c], **Swagata Acharya**[d], **Thomas Brumme**[c,e], **Evgeniia Sheveleva**[f], **Fryderyk Lyzwa**[f], **Ekaterina Pomjakushina**[g], **Christian Bernhard**[f], **Mark van Schilfgaarde**[d], **Fabrizio Carbone**[a], **Angel Rubio**[c,h,i,1], **and Cédric Weber**[d,1]

[a]Institute of Physics, Laboratory for Ultrafast Microscopy and Electron Scattering, École Polytechnique Fédérale de Lausanne, CH-1015 Lausanne, Switzerland; [b]Institute of Chemical Sciences and Engineering, Laboratory of Ultrafast Spectroscopy, École Polytechnique Fédérale de Lausanne, CH-1015 Lausanne, Switzerland; [c]Max Planck Institute for the Structure and Dynamics of Matter, D-22761 Hamburg, Germany; [d]Department of Physics, King's College London, London WC2R 2LS, United Kingdom; [e]Wilhelm Ostwald Institut of Physical and Theoretical Chemistry, University of Leipzig, D-04103 Leipzig, Germany; [f]Department of Physics, University of Fribourg, Chemin du Musée 3, CH-1700 Fribourg, Switzerland; [g]Solid State Chemistry Group, Laboratory for Multiscale Materials Experiments, Paul Scherrer Institute, CH-5232 Villigen PSI, Switzerland; [h]Nano-Bio Spectroscopy Group, Departamento de Física de Materiales, Universidad del País Vasco, 20018 San Sebastían, Spain; [i]Center for Computational Quantum Physics, The Flatiron Institute, 162 Fifth Avenue, New York, NY 10010, USA

S1. Steady-state Optical Data

We simultaneously fitted the measured real (ϵ_1) and imaginary (ϵ_2) parts of the dielectric function along each polarization channel at 10 K with a Lorentz model. In this approach, Lorentz oscillators are used to describe the contribution of the interband transitions to the dielectric response. The analytical expression of ϵ_1 and ϵ_2 of the Lorentz functions can be found elsewhere (1). The combined fit of ϵ_1 and ϵ_2 provides an accurate description of the optical quantities in the energy range of interest and it is crucial to overcome the issues related to a Kramers-Kronig analysis of the transient reflectivity data. The results of the fit are shown in Fig. S1 *A* and *B* as solid lines. Along the *a*-axis, we find that the relevant oscillators contributing to the spectral region over which our pump-probe experiment is sensitive are centered at $a_1 = 1.73$ eV, $a_2 = 2.16$ eV and $a_3 = 2.64$ eV. Oscillator a_1 well agrees with the energy of a *d*-*d* crystal field excitation reported by optical spectroscopy (2, 3) and resonant inelastic x-ray scattering (4). Oscillator a_2 is the excitation across the optical charge-transfer (CT) gap, whereas oscillator a_3 represents the high-energy shoulder to the optical CT excitation (2–4). Over the same energy region along the *c*-axis, Lorentz oscillators are instead centered at c_1 = 1.49 eV and $c_2 = 4.08$ eV.

S2. Temperature Dependence of the Optical Properties

In this Section, we show how the optical properties of LCO respond to an increase in the lattice temperature. This analysis allows us to identify any thermal response in the pump-probe experiment.

First, we estimate the maximum transient lattice temperature that is reached in a crystal of LCO upon photodoping with the maximum excitation density used in our pump-probe experiment. To this aim, we rely on the simple expression

$$Q = \int_{T_i}^{T_f} mC(T)\delta T \qquad [1]$$

where Q is the absorbed heat from a single laser pulse, m is the illuminated mass, $C(T)$ is the temperature-dependent specific heat, $T_i = 10$ K is the initial equilibrium temperature, and T_f is the final temperature. We use our photoexcited carrier density values and calculate m through the material density $\rho = 6.92$ g/cm^3 and the illuminated sample volume $V = 4 \times 10^{-9}$ cm^3. We consider the temperature dependence of the heat capacity, as measured at low temperature in Ref. (5) and extrapolated to high temperature with a linear behavior. At the minimum excitation density used in the experiments the calculation yields $T_{f,min} = 79$ K, whereas at the maximum excitation density we obtain $T_{f,max} = 128.5$ K. The latter temperature is still well below the Néel temperature of our sample ($T_N = 307$ K).

As a second step, we measure the temperature dependence of the optical response via spectroscopic ellipsometry along the *a*- and *c*-axis between 10 K and 300 K. The data are shown in Figs. S2 $A - F$. In the following, we restrict the visualization of the data only to the spectral region that is relevant to our pump-probe experiment. An interpolation procedure is applied to increase the number of data points and improve the presentation of the changes induced in the optical spectra by the temperature increase.

The real and imaginary part of the *a*-axis optical conductivity are shown in Figs. S2 *A* and *B* at 10 K and 150 K. We observe that the optical CT excitation in σ_{1a} broadens and redshifts with increasing temperature, in agreement with previous studies (2). The inset of Fig. S2 *A* zooms in the evolution of the optical CT feature close to the peak energy: The crossing point between each of the high-temperature traces and that at 10 K also redshifts with increasing temperature, as indicated by the arrows. As a result, the temperature-driven differential conductivity $\Delta\sigma_{1a}$ (brown curve in Fig. S2 *C*) shows a positive feature at lower energy, followed by a negative one at higher energy. This is again consistent with previous reports (6, 7). The same temperature increase also influences σ_{2a} (which is < 0), yielding a sizable decrease of its absolute value over the 1.90-2.30 eV energy range. In this case, the differential conductivity $\Delta\sigma_{2a}$ (violet curve in Fig. S2 *C*) results in a positive contribution.

We now focus on the *c*-axis optical response. Here, since the optical quantities are rather temperature independent in the 10-150 K range, we compare the response at 10 K with that at 300 K. This allows us to enhance the contrast to visualize the temperature-induced variation of the optical quantities. In Fig. S2 *D*, we observe that σ_{1c} is slightly reduced with

increasing temperature, which implies a negative $\Delta\sigma_{1c}$ (brown curve in Fig. S2 *F*). Furthermore, the absolute value of σ_{2c} (Fig. S2 *D*) increases over the the 1.90-2.50 eV range. The resulting $\Delta\sigma_{2c}$ has a negative sign (violet curve in Fig. S2 *F*).

S3. Estimation of the Time Resolution in the Pump-probe Data

We also estimate the temporal resolution of our ultrafast experiments by identifying a resolution-limited rise in the ΔR/R temporal traces. This is shown in Fig. S3, where the temporal trace is selected around 2.60 eV in the *c*-axis probe polarization channel. We observe an ultrafast rise of ∼50 fs (peak-to-peak) in the transient response, which is a clear fingerprint of the time-resolution of our experimental setup. The same apparatus was used in several studies to generate and detect coherent optical phonons (with energies as high as 70 meV) in other materials (8–12).

S4. Comparison with Other Materials

In this Section, we show that the ultrafast response observed in the rise of the LCO temporal traces is an intrinsic property of this material and not an artifact produced by our experimental setup. To this aim, we measure other samples under the same experimental conditions, namely a thin film of the anisotropic metal MgB_2 and a single crystal of the band semiconductor $CH_3NH_3PbBr_3$. We excited both materials with a 45 fs laser pulse centered around 3.10 eV and monitored the pump-probe response with the same time step utilized to measure LCO (∼13 fs). The ΔR/R temporal response from the different materials is shown in Fig. S4. Here for simplicity we select the temporal traces around a photon energy of 2.45 eV, but the results are general and apply to the whole measured spectral range and for different pump fluences. We observe that only the temporal traces of LCO show a resolution-limited signal before 0.17 ps, whereas the rise time in MgB_2 and $CH_3NH_3PbBr_3$ is significantly slower and corresponds to the results reported in the literature with similar excitation schemes (13, 14). These findings rule out the involvement of a material-independent optical nonlinearity in the ultrafast signal of LCO.

S5. Transient Reflectivity

Figures S5 *A* and *C* display the color-coded maps of the ΔR/R response as a function of the probe photon energy and of the time delay between pump and probe at 10 K, for a probe polarization along the *a*- and *c*-axis, respectively. In both cases, the pump polarization is set along the *a*-axis and the excitation density is estimated at 0.06 photons/Cu. The *a*-axis ΔR/R response (Fig. S5 *A*) shows a negative feature centered around 2.15 eV, which corresponds to the optical CT excitation. This response is consistent with that of previous studies of the in-plane charge dynamics (7, 8). Unlike the signal obtained upon below-gap excitation, here the response is one order of magnitude larger due to the enhanced absorption of particle-hole pairs across the optical CT gap. In addition, the high-energy region of the spectrum displays a sign inversion around 0.5 ps, as evident from the time traces in Fig. S5 *B*.

The *c*-axis ΔR/R response in Fig. S5 *C* shows instead a more complex behavior, with two distinct regions of negative and positive photoinduced changes. These features are well displayed by selecting specific temporal traces across the probed spectral range, as evidenced in Fig. S5 *D*. Again, an extremely fast signal appears in the rise of the response during the first hundred of femtoseconds. The subsequent relaxation dynamics consists of a multi-exponential decay. On top of this background, a prominent oscillatory pattern clearly emerges across the whole spectrum.

To unravel the degree of anisotropy governing the *a*- and *c*-axis response, we compare two temporal traces selected from the color-coded maps of Figs. S5 *A* and *C*. The results are shown in Fig. S6 *A* and *B*, in which the traces have been normalized for comparison. It is evident that the *c*-axis relaxation dynamics is faster than its *a*-axis counterpart, which represents a signature of a more insulating behavior shown by the out-of-plane charge transport. We also observe that, in the in-plane dynamics, the high signal intensity resulting from the optical CT excitation hides a clear manifestation of the coherent oscillations. In contrast, in the out-of-plane dynamics, a beating among several coherent modes is clearly distinguished and found to persist up to several picoseconds. Despite this difference in the relaxation, the rise time of both traces is found to be identical within our experimental resolution, as shown in Fig. S6 *B*. This indicates that the same phenomenon governs the rise time along the two crystallographic axes of LCO.

S6. Transient Optical Conductivity

From our nonequilibrium experiment we extract the transient complex optical conductivity $\Delta\sigma(\omega,t) = \Delta\sigma_1(\omega, t) + i\,\Delta\sigma_2(\omega, t)$. This can be calculated without the need of a Kramers-Kronig analysis by relying on our steady-state spectroscopic ellipsometry data of Fig. S1 as a starting point and performing a differential Lorentz model of the ΔR/R maps. This method has been previously utilized to treat ultrafast broadband optical data (15, 16) and it represents the most accurate procedure currently developed.

To extract $\Delta\sigma(\omega,t)$ from the ΔR/R data, we proceed as follows. We use the static reflectivity R determined via spectroscopic ellipsometry and obtain the momentary reflectivity $R(\omega,t)$ in the range explored by the pump-probe experiment by multiplying $\Delta R/R(\omega,t)$ at a fixed time delay t by R itself. As starting parameters, we use those describing the steady-state response of Fig. S1. Letting one (two) Lorentz oscillator(s) free to vary in the frequency range along the *a*-axis (*c*-axis) is sufficient to accurately reproduce the $R(\omega,t)$ spectra at all times delays. In a final step, the transient optical conductivity spectra $\Delta\sigma_1(\omega, t)$ and $\Delta\sigma_2(\omega, t)$ are recombined into the full maps of Fig. S8.

The long temporal window covered by our experiment at high time resolution allow us to refine the model of Okamoto *et al.* (6) and extract information about the dynamics along the *a*- and *c*-axis. We find that both responses can be fitted only with the equation below. The first term describes a pulsed response that captures the fast dynamics related to the metallic state. The second term comprises distinct exponential relaxation processes (i = 3 for the in-plane response and i = 2 for the out-of-plane response) due to the decay of the metallic state and the charge localization in mid-gap states. The last delayed component corresponds to the bolometric (heating) response of the sample, which sets after the thermalization of the excited carriers has occurred. $\tau_{R_1} = 0.01 \pm 0.001$ ps is the

$$f(t) = C_G \exp\left(\frac{-(t-D)^2}{\tau_{R_1}}\right) + \sum_i C_i \int_{-\infty}^{t} \exp\left(-\frac{t-t'}{\tau_i} - \frac{(t-D)^2}{\tau_{R_1}}\right) dt' +$$
$$+ C_H \int_{-\infty}^{t} \left[1 - \exp\left(-\frac{t-t'}{\tau_{R_2}}\right)\right] \exp\left(-\frac{t-t'}{\tau_H} - \frac{(t-D)^2}{\tau_{R_2}}\right) dt'$$

rise time of the Gaussian term, whereas $\tau_{R_2} = 0.03 \pm 0.0003$ ps is the rise time of the exponential components.; τ_i are the relaxation constants of the exponential decays; D is a delay parameter with respect to the zero time. The results of the fit are shown in Fig. S9 *A* and *B* as dashed black lines superposed on the original data. The timescales obtained along the *a*-axis are $\tau_1 = 0.06 \pm 0.002$ ps, $\tau_2 = 0.4 \pm 0.003$ ps, $\tau_3 = 1 \pm 0.008$ ps, and $\tau_H = 0.65 \pm 0.07$ ps, while those along the *c*-axis are $\tau_1 = 0.06 \pm 0.004$ ps, $\tau_2 = 1.9 \pm 0.01$ ps, and $\tau_H = 3 \pm 1.85$ ps. The fact that both fits along the *a*- and *c*-axis indepentently provide the same values for τ_{R_1} and τ_{R_2} strongly supports the idea (already evident from the inspection of the raw data) that the same ultrafast phenomenon (namely the ultrafast metallic state) emerges along both crystallographic directions.

S7. Photon Energy Dependence of the Collective Modes' Amplitudes

In this Section, we benefit from the use of a broadband continuum probe to extract the photon energy dependence of the oscillation amplitude for four distinct Raman-active modes in the pump-probe experiment. To this aim, we focus on the ΔR/R response along the material's *c*-axis, along which the oscillations emerge clearly. We select twenty temporal traces from the map displayed in Fig. S5 *C* and perform a global fit analysis by imposing the same relaxation time constants across the monitored spectral region. By calculating the Fourier transform of the residuals, for each collective mode we reconstruct its intensity profile, as shown in Fig. S12. The low intensity of mode $A_g(5)$ prevented us from extracting its photon energy dependence. Similar results were obtained by decreasing the excitation density to 0.023 ph/Cu, which is still above the threshold to induce the metallic state in LCO (6).

As evident from Fig. S12, the oscillatory response of the in-plane pump/out-of-plane probe data is dominated by the optical phonon $A_g(3)$, which corresponds to the in-phase vibration between La and apical O atoms. The intensity of this mode shows a first feature around 2.00 eV, followed by a marked increase above 2.50 eV. The strong enhancement of the mode intensity towards high energies agrees with the idea that the *c*-axis electrodynamics in the 2.60-3.00 eV spectral region is dominated by transitions from Cu to apical O states (17–19). Interestingly, this mode was also found to oscillate in the *c*-axis ΔR/R response of optimally-doped $La_{1.85}Sr_{0.15}CuO_4$ upon in-plane photoexcitation at 1.55 eV (18, 20). Consistent with our measurements, also in $La_{1.85}Sr_{0.15}CuO_4$ this phonon was found to resonate at an energy scale above 2.50 eV.

Mode $A_g(4)$, corresponding to the vibrations of the in-plane O along the *c*-axis, produces a sizable effect in the region between 1.80 and 2.50 eV and resonates around 2.00 eV. This resonant enhancement around 2.00 eV allows us to conclude that the underlying interband transition is modulated by displacements along the *c*-axis of the material. Thus, the origin of this interband transition may lie in the transfer of a hole from a Cu atoms to a planar O of a contiguous plane. The estimate of the Madelung energy for such a process ($\sim$ 2.00 eV) supports this scenario (18).

The complete mapping of the Raman profiles along the *c*-axis opens perspectives towards the evaluation of the electron-phonon matrix elements for all A_g modes of LCO in future *ab initio* calculations.

S8. Additional QSGW+DMFT Results

The compound with undisplaced unit cell has been recently characterized by the local density approximation (LDA) and the quasiparticle self-consistent GW + dynamical mean-field theory (QSGW+DMFT) methods (see Ref. (21)). The LDA bands at the Fermi level consist of strongly mixed (3:2) Cu-3$d_{x^2-y^2}$ and O-2p_x, p_y orbitals. The Cu-3d_{z^2} orbitals also have strong mixing with primarily apical O-2p_z orbital at 1.90 eV below the Fermi level. The O-2p states are strongly hybridized with most orbital characters throughout the entire window $[E_F - 8\,\text{eV}, E_F]$. However, unlike in LDA, the self-energy in QSGW (the off-diagonal, dynamic and momentum-dependent matrix elements) splits out the O-2p orbitals from the Cu-3d ones and puts them roughly 2 eV below the band with dominant Cu 3d_{z^2} character. Within the QSGW description, the band character at the Fermi level becomes predominantly Cu-3$d_{x^2-y^2}$, with significantly lessened O-2p_x, p_y contribution than in LDA. In particular, the QSGW bands closest to the Fermi level consist of 2:1 admixtures of Cu-3$d_{x^2-y^2}$ and O-2p_x, p_y orbitals. However, we find that the QSGW band at the Fermi level has finite but small contribution from the Cu-4s orbital on the $A-C_0-E_0$ and $S-R-Z$ symmetry lines. Its weight is more pronounced near the Y point, in a band with Cu-4s character. O-2p_z below -3 eV hybridize to some extent with Cu-3d_{z^2} around -2 eV and the other Cu-3d orbitals, and to a lesser extent, the bands at E_F.

The main advantage of non-magnetic QSGW bands for the displaced structure of LCO is to get rid of the f-states (otherwise present in density-functional theory calculations) from the spectral region close to Fermi energy. Furthermore, the off-diagonal orbital elements of QSGW self-energy makes the Cu-3$d_{x^2-y^2}$ character prominent in the active band at the Fermi energy and it also controls the relative orientations of different O and Cu-3d_{z^2} states with respect to the Cu-3$d_{x^2-y^2}$ ones (21). Relative orientations of different Cu-3d states and in-plane O-2p and apical O-2p states are tabulated in Table I. On analyzing the bare energies for different orbitals presented in the Table I, we find that there is no clear trend in the change in CT energies that distinguishes the B_g modes from the A_g modes. On average, all Raman-active modes simulate a change in in-plane and out-of-plane CT energies by $\sim$30-40 meV. However, the electronic structure for LCO displaced along the $A_g(3)$ mode coordinates is characterized by an apical

O-p_z state that is nearly degenerate with the Cu-3d_{z^2}. In the electronic structure for LCO displaced along the $A_g(5)$ mode eigenvector, the Cu-3$d_{x^2-y^2}$-3d_{z^2} splitting reduces by ∼130 meV and the in-plane CT energy drops by ∼70 meV. Moreover, the apical O-p states are fairly closer to the $d_{x^2-y^2}$ state in the electronic structure of LCO displaced along the $A_g(2)$ and $A_g(5)$ modes. Finally, in the electronic structure obtained upon displacements along the B_{1g} and B_{2g} modes, the in-plane CT energy increases by ∼30-40 meV.

Once QSGW is coupled with DMFT, the local dynamical spin fluctuations put the system on the brink of a Mott transition. Irrespective of whether the modes are A_g or B_g, the low-energy properties cannot be characterized in a purely Bloch band-like scenario. When the unit cell is displaced along the B_g modes eigenvectors, the system appears to evolve through a local dynamic IMT with an imaginary part of the local self-energy that picks up a pole at low energies ($\omega \sim 0$), effectively suppressing the low-energy quasiparticle excitation. However, in the case of the B_{3g} mode, incoherent excitations can be observed across the Fermi energy, while quasiparticle-like excitations are absent. An incoherent metal with large effective mass characterizes the electronic structure of the system displaced along the A_g modes' coordinates. Displacements along $A_g(1)$ lead to a single-particle response that is similar to the one for the compound displaced along the B_{3g} mode. However, for other A_g modes at low energy, it is still possible to perform low-energy quasiparticle fittings. In these cases, the QSGW+DMFT electronic spectral functions show a three-peak structure that is typically found in the strong coupling regime of correlated electron systems; both the incoherent, heavy quasiparticle excitation at low energy and atomic-like Hubbard "band" features at high energy can be observed. The lower Hubbard band is extremely broad and spreads over ∼6-8 eV, in excellent agreement with the data reported in Ref. (22). The bad metallic nature of the broad incoherent quasiparticle excitation present at $\omega = 0$ can be characterized for the different A_g modes by computing the mass enhancement factor (m^*/m) and single-particle scattering rate (γ). The results are listed in Table II. In the last column of Table II, we show the effective doping concentration in the Cu-3d states when the unit cell of LCO is displaced along the different Raman-active modes. We observe that the modes that provide more metallicity simulate a stronger effective doping (hole doping in case of A_g modes and electron doping in case of B_{3g} mode) in the Cu-3d states. However, the total electron count for the the structures displaced along all Raman-active modes is the same, and the systems are not doped in reality. The effective doping in B_{1g} and B_{2g} modes is almost negligible in comparison to undisplaced LCO.

Supplementary References

1. Jellison Jr GE, et al. (2000) Characterization of thin-film amorphous semiconductors using spectroscopic ellipsometry. *Thin Solid Films* 377:68–73.
2. Falck JP, Levy A, Kastner MA, Birgeneau RJ (1992) Charge-transfer spectrum and its temperature dependence in La_2CuO_4. *Phys. Rev. Lett.* 69(7):1109.
3. McBride JR, Miller LR, Weber WH (1994) Ellipsometric study of the charge-transfer excitation in single-crystal La_2CuO_4. *Phys. Rev. B* 49(17):12224.
4. Ellis DS, et al. (2008) Charge-transfer exciton in La_2CuO_4 probed with resonant inelastic x-ray scattering. *Phys. Rev. B* 77(6):060501.
5. Jorge GA, et al. (2004) Thermodynamic properties of excess-oxygen-doped $La_2CuO_{4.11}$ near a simultaneous transition to superconductivity and long-range magnetic order. *Phys. Rev. B* 69(17):174506.
6. Okamoto H, et al. (2011) Photoinduced transition from Mott insulator to metal in the undoped cuprates Nd_2CuO_4 and La_2CuO_4. *Phys. Rev. B* 83(12):125102.
7. Novelli F, et al. (2014) Witnessing the formation and relaxation of dressed quasi-particles in a strongly correlated electron system. *Nat. Commun.* 5:5112.
8. Mann A, et al. (2015) Probing the electron–phonon interaction in correlated systems with coherent lattice fluctuation spectroscopy. *Phys. Rev. B* 92(3):035147.
9. Mann A, et al. (2016) Probing the coupling between a doublon excitation and the charge-density wave in TaS_2 by ultrafast optical spectroscopy. *Phys. Rev. B* 94(11):115122.
10. Baldini E, et al. (2017) Clocking the onset of bilayer coherence in a high-T_C cuprate. *Phys. Rev. B* 95(2):024501.
11. Borroni S, et al. (2017) Coherent generation of symmetry-forbidden phonons by light-induced electron–phonon interactions in magnetite. *Phys. Rev. B* 96(10):104308.
12. Baldini E, et al. (2018) Lattice-mediated magnetic order melting in $TbMnO_3$. *Phys. Rev. B* 97(12):125149.
13. Baldini E, et al. (2017) Real-time observation of phonon-mediated σ-π interband scattering in MgB_2. *Phys. Rev. Lett.* 119(9):097002.
14. Palmieri T, et al. (2020) Mahan excitons in room-temperature methylammonium lead bromide perovskites. *Nat. Commun.* 11:850.
15. Mansart B, et al. (2012) Evidence for a Peierls phase-transition in a three-dimensional multiple charge-density waves solid. *Proc. Natl. Acad. Sci.* 109(15):5603–5608.
16. Novelli F, et al. (2012) Ultrafast optical spectroscopy of the lowest energy excitations in the Mott insulator compound YVO_3: Evidence for Hubbard-type excitons. *Phys. Rev. B* 86(16):165135.
17. Uchida S, et al. (1991) Optical spectra of $La_{2-x}Sr_xCuO_4$: Effect of carrier doping on the electronic structure of the CuO_2 plane. *Phys. Rev. B* 43(10):7942.
18. Lorenzana J, et al. (2013) Investigating pairing interactions with coherent charge fluctuation spectroscopy. *Eur. Phys. J. Special Topics* 222(5):1223–1239.
19. Uchida S, Tamasaku K, Tajima S (1996) c-axis optical spectra and charge dynamics in $La_{2-x}Sr_xCuO_4$. *Phys. Rev. B* 53(21):14558.
20. Mansart B, et al. (2013) Coupling of a high-energy excitation to superconducting quasiparticles in a cuprate from coherent charge fluctuation spectroscopy. *Proc. Natl. Acad. Sci.* 110(12):4539–4544.
21. Acharya S, et al. (2018) Metal-insulator transition in copper oxides induced by apex displacements. *Phys. Rev. X* 8(2):021038.
22. Nücker N, et al. (1987) Experimental electronic structure studies of $La_{2-x}Sr_xCuO_4$. *Zeit. Phys. B Cond. Matt.* 67(1):9–14.

Mode	Cu-3$d_{x^2-y^2}$	Cu-3d_{z^2}	apical O-2p_y	AO-2p_z	AO-2p_x	IO-2p_y	IO-2p_z	IO-2p_x
Undisplaced	0.000000	-0.729280	-0.212671	-0.493781	-0.199210	-1.486084	-0.929154	-1.484877
A_g(1)	0.000000	-0.707354	-0.261992	-0.481159	-0.228354	-1.485348	-0.921401	-1.477706
A_g(2)	0.000000	-0.751029	-0.154252	-0.452560	-0.156449	-1.519043	-0.932744	-1.508519
A_g(3)	0.000000	-0.718872	-0.400241	-0.719047	-0.399869	-1.483198	-0.928412	-1.479216
A_g(4)	0.000000	-0.684008	-0.239187	-0.534775	-0.206341	-1.488909	-0.916818	-1.486509
A_g(5)	0.000000	-0.591483	-0.086867	-0.364024	-0.079538	-1.415804	-0.851139	-1.413909
B_{1g}	0.000000	-0.681711	-0.253692	-0.513599	-0.248558	-1.509005	-0.948838	-1.513572
B_{2g}	0.000000	-0.657151	-0.315573	-0.562927	-0.277567	-1.534287	-0.978037	-1.530722
B_{3g}	0.000000	-0.686722	-0.184135	-0.460328	-0.165544	-1.494214	-0.920689	-1.494236

Table S1. Relative energies of different orbitals with respect to the Cu-3$d_{x^2-y^2}$. All numbers are given in eV. AO = apical oxygen; IO = in-plane oxygen.

Mode	m^*/m	γ (meV)	Effective Cu-3d doping (δ)
A_g(1)	24	100	0.7%
A_g(2)	19	26	3.5%
A_g(3)	24	15	2.7%
A_g(4)	13	21	3.4%
A_g(5)	12	11	3.3%
B_{1g}			0.4%
B_{2g}			0.3%
B_{3g}			-1.6%

Table S2. Quasiparticle mass enhancement factor (m^*/m), scattering rate (γ) for the metallic state resulting from the displacement of the unit cell of LCO along different A_g and B_g mode coordinates. Effective Cu-3d level hole doping (negative sign for B_{3g} mode implies electron doping) are presented in the last column.

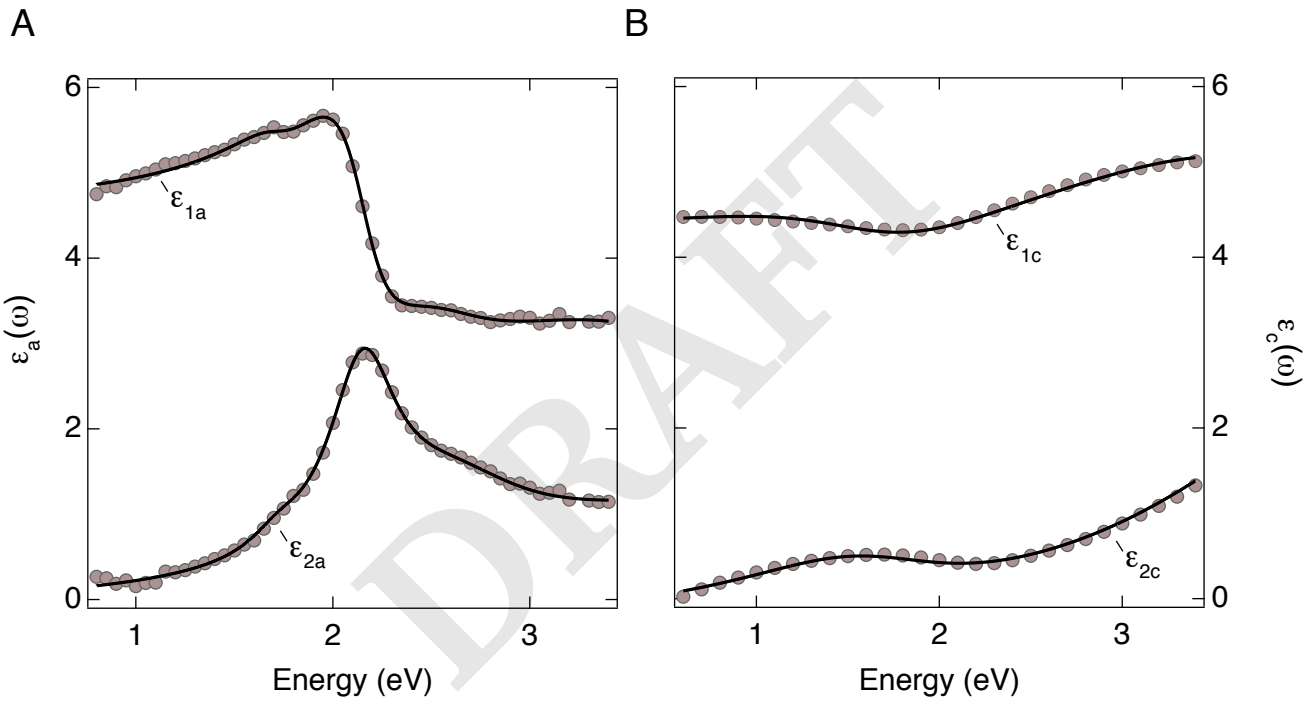

Fig. S1. *(A,B)*, Real ($\epsilon_1(\omega)$) and imaginary ($\epsilon_2(\omega)$) parts of the complex dielectric function of LCO, measured at 10 K with spectroscopic ellipsometry (brown dots) along the (A) a-axis and (B) c-axis. Solid lines show fits of the measured data to a Lorentz model.

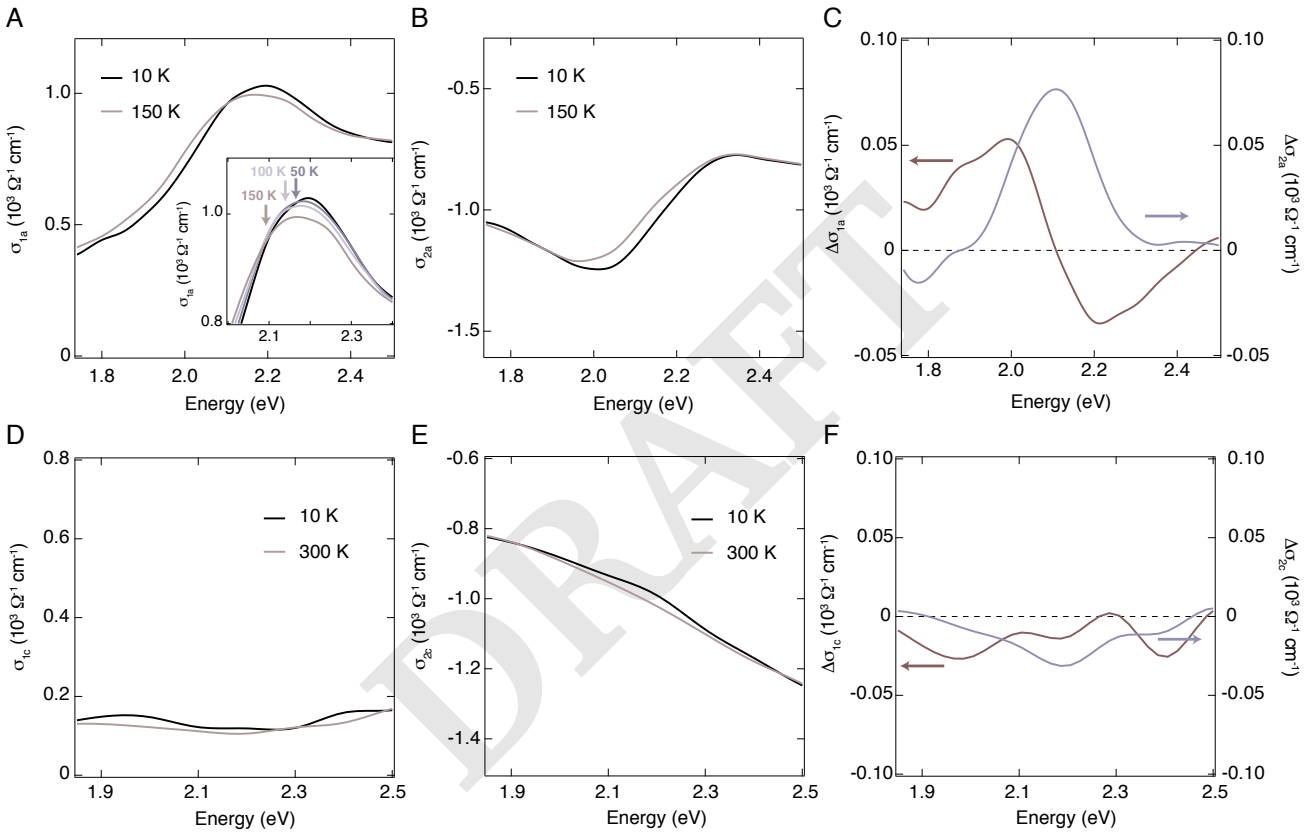

Fig. S2. Temperature dependence of the real ($\sigma_1(\omega)$) and imaginary ($\sigma_2(\omega)$) parts of the complex optical conductivity of LCO. *(A,B)*, Optical response along the a-axis (inset of Panel (A) zooms in the region of the optical CT feature). *(C)*, Differential optical conductivity along the a-axis when the temperature is varied from 10 K to 150 K ($\Delta\sigma_a$ = σ_a(150 K) - σ_a(10 K)). *(D,E)*, Optical response along the c-axis. *(F)* Differential optical conductivity along the c-axis when the temperature is varied from 10 K to 300 K ($\Delta\sigma_c$ = σ_c(300 K) - σ_c(10 K)).

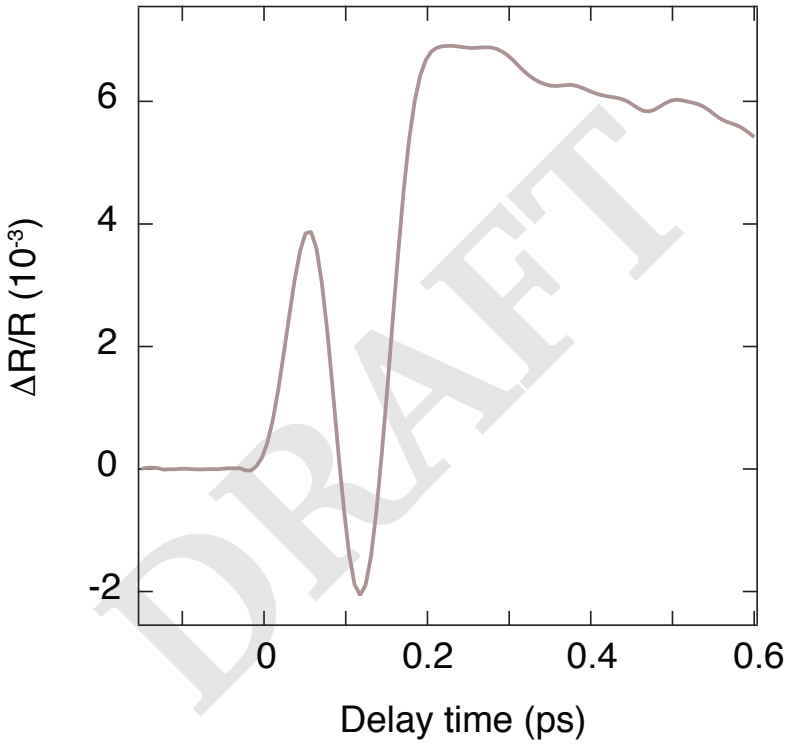

Fig. S3. Estimate of the temporal resolution of the pump-probe experiment. The temporal trace shown is selected at a photon energy of 2.60 eV in the experiment with pump polarized along the a-axis and probe polarized along the c-axis. The rise of the trace is resolution-limited and the time resolution can be estimated around $\sim$0.05 ps.

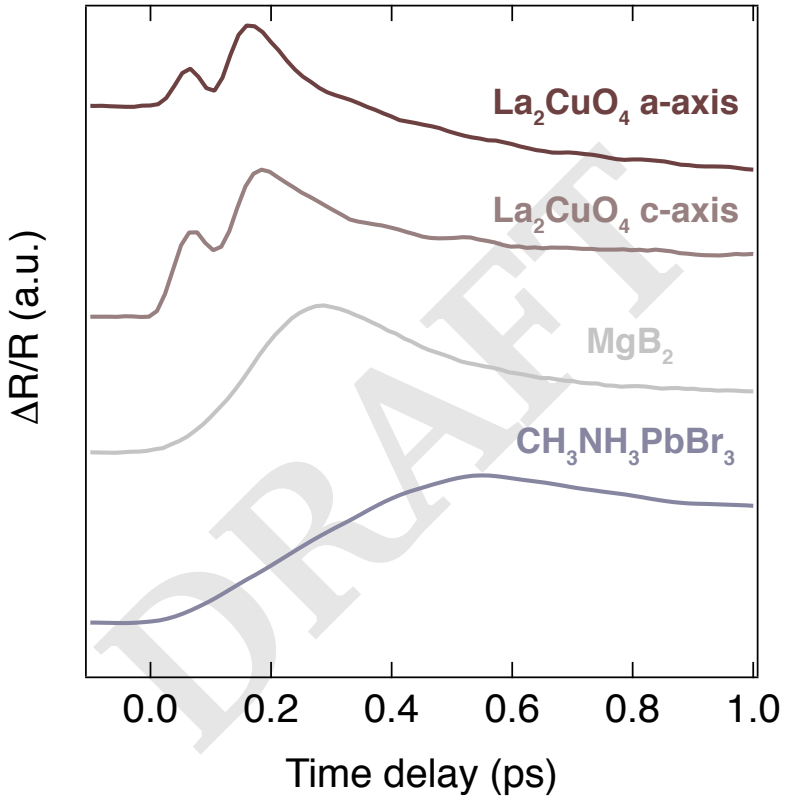

Fig. S4. Normalized ΔR/R data measured on different materials photoexcited with 45 fs laser pulses at 3.10 eV. The temporal traces were integrated over 0.10 eV around the probe photon energy of 2.45 eV, but the results are general and apply to the whole measured spectral range ($\sim$1.74-2.60 eV). The comparison is made between LCO single crystals with probe polarization along the a- and c-axis (brown curves), MgB_2 thin films (green curve) and $CH_3NH_3PbBr_3$ single crystals (violet curve). Only LCO responds to photoexcitation with an extremely fast signal during the first 0.1 ps, indicating that this is an intrinsic material property. For clarity, the LCO response along the a-axis has been multiplied by -1.

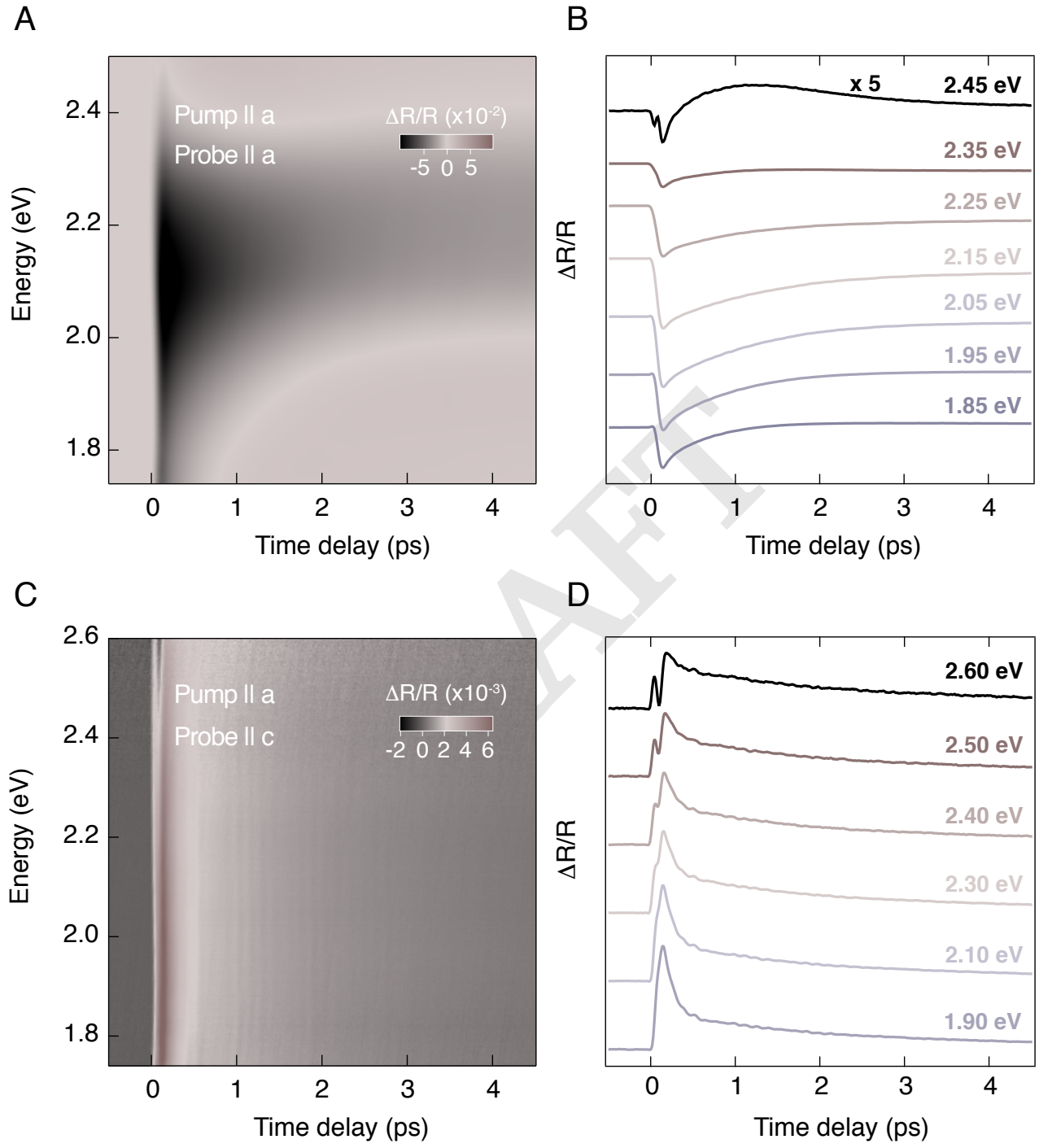

Fig. S5. (*A,C*) Color-coded maps of ΔR/R at 10 K with in-plane pump polarization and (A) in-plane, (C) out-of-plane probe polarization, as a function of probe photon energy and pump-probe time delay. The pump photon energy is 3.10 eV and the excitation density is 0.06 photons/Cu. *(B,D)* Temporal traces at specific probe photon energies of the respective ΔR/R maps. Each temporal trace results from the integration over 0.10 eV around the indicated probe photon energy.

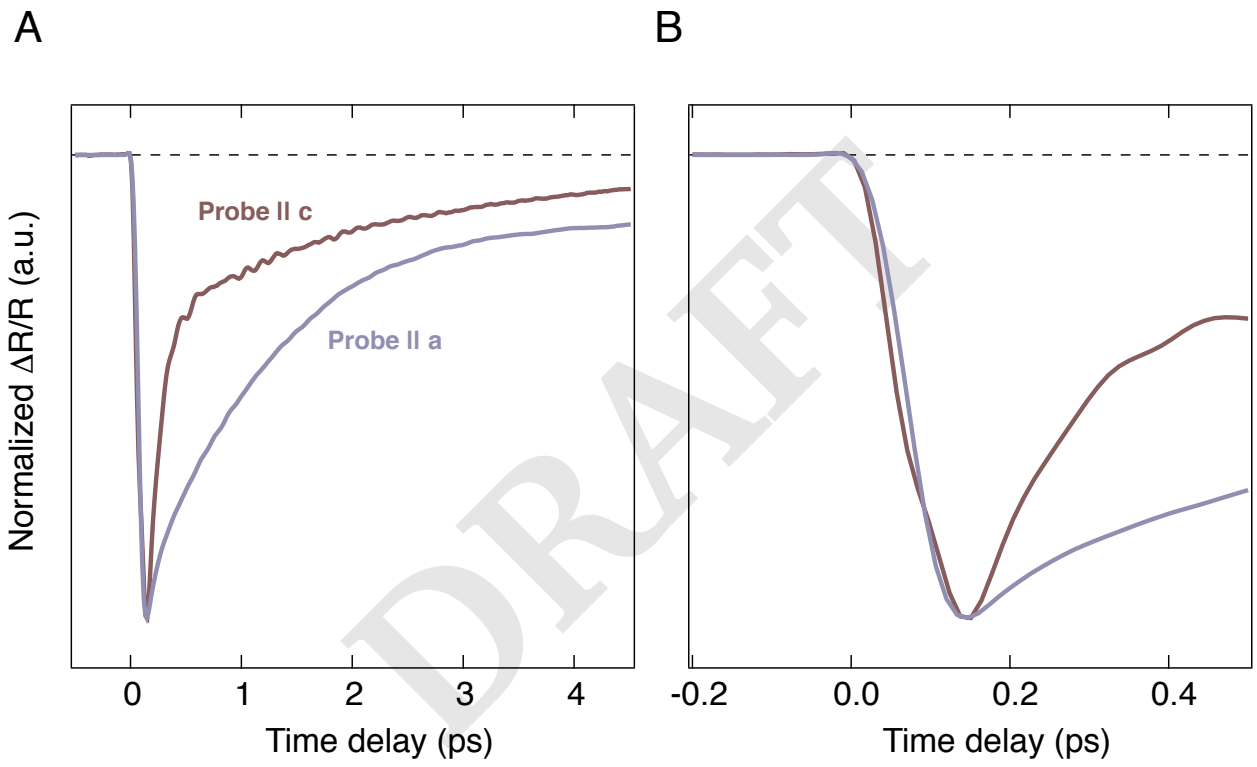

Fig. S6. Comparison between the in-plane (violet trace) and out-of-plane (brown trace) temporal evolution of $\triangle$R/R upon in-plane photoexcitation. The traces have been normalized to enable comparison and the sign of the out-of-plane response has been reversed. To maximize the signal-to-noise ratio, the in-plane temporal trace has been selected at a photon energy of 2.10 eV and integrated over 0.20 eV, whereas the out-of-plane trace is cut at 2.00 eV and integrated over 0.40 eV. The excitation density is 0.06 photons/Cu. *(A)*, Complete temporal response. *(B)*, Zoom into the rise time of the response.

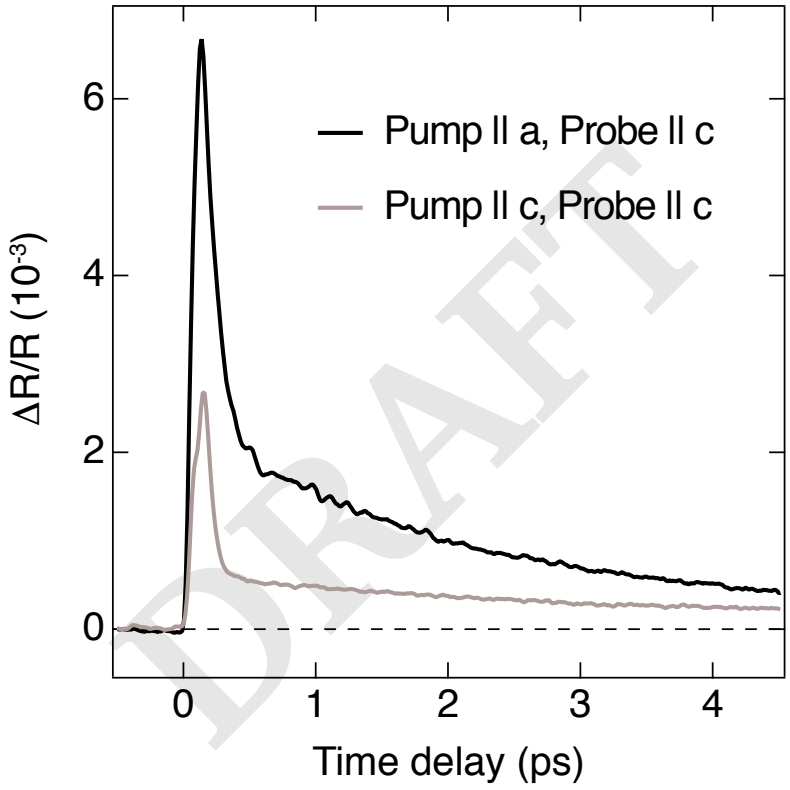

Fig. S7. Out-of-plane $\triangle$R/R temporal response for a pump polarization set along the a-axis (black curve) and c-axis (brown curve). The carrier excitation density is kept constant between the two excitation schemes (0.06 photons/Cu) by relying on the steady-state optical response of LCO. Both traces are obtainted from the integration over 0.10 eV around a photon energy of 1.80 eV. We observe that the signal resulting from out-of-plane photoexcitation has a weaker amplitude than the one obtained from in-plane photoexcitation and the signature of the coherent phonon modes also changes dramatically between the two pump polarization configurations.

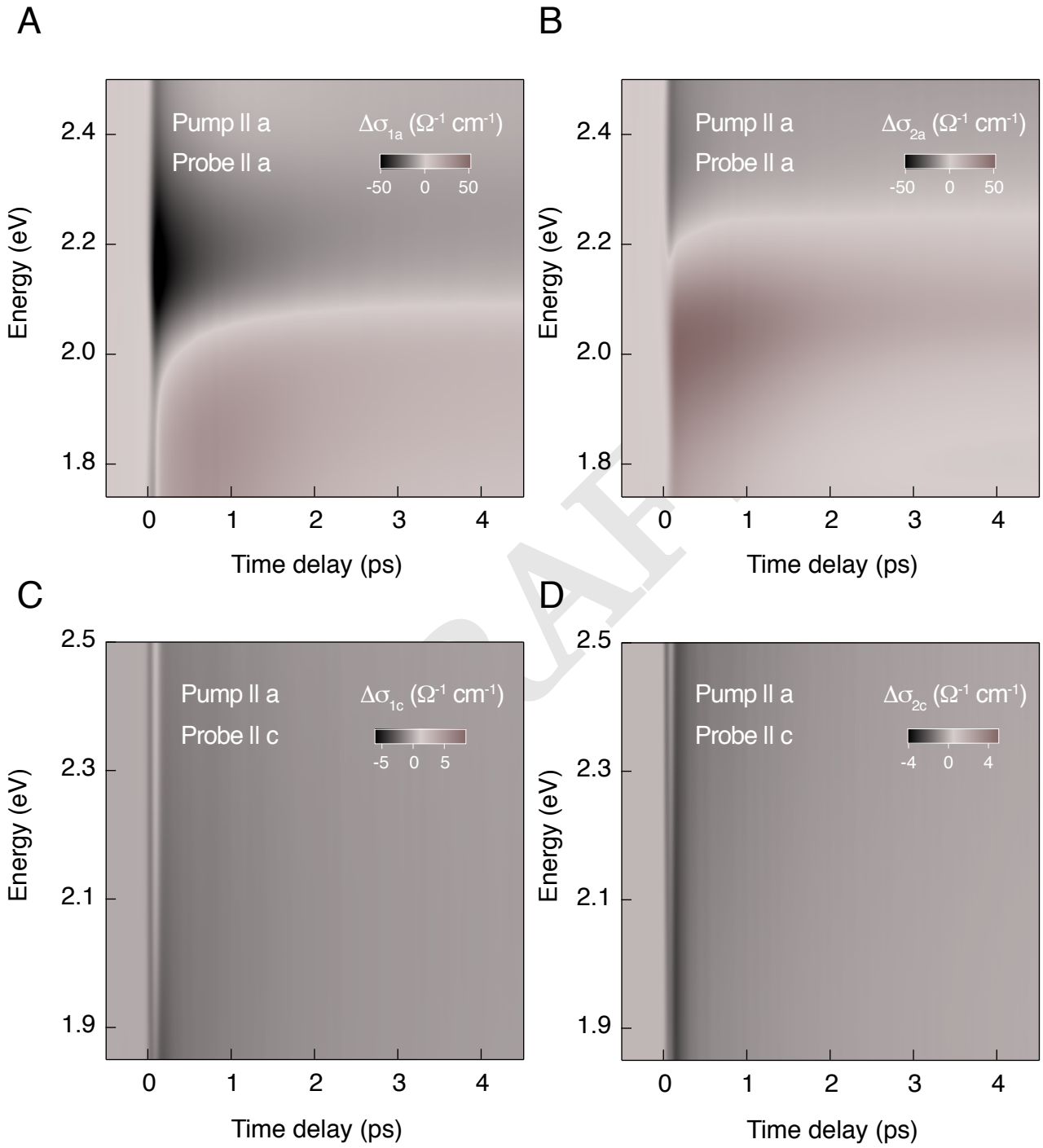

Fig. S8. Color-coded maps of the real ($\Delta\sigma_1$) and imaginary ($\Delta\sigma_2$) part of the complex optical conductivity at 10 K with a-axis pump polarization and *(A,B)*, a-axis, *(C,D)*, c-axis probe polarization. The pump photon energy is 3.10 eV and the excitation density is 0.06 photons/Cu.

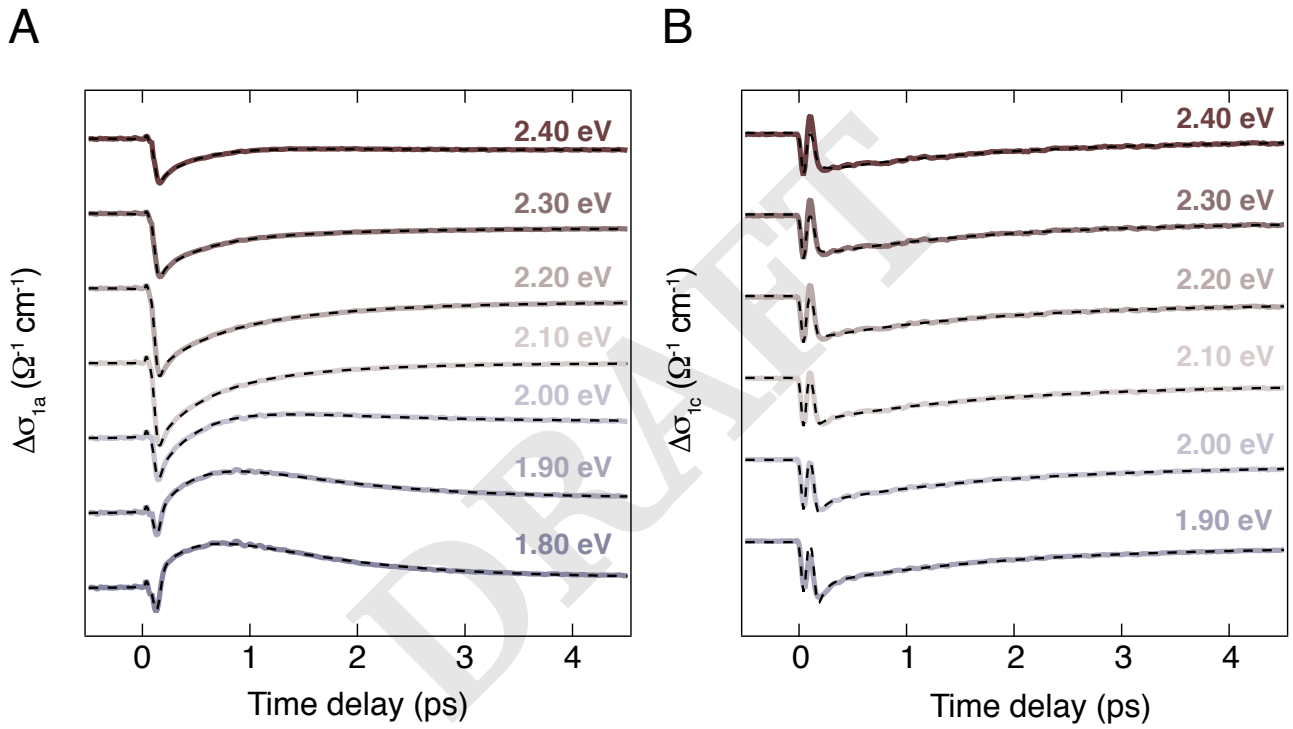

Fig. S9. Global fit analysis of the $\Delta\sigma_1$ temporal traces along the *(A)*, a-axis, and *(B)*, c-axis. The solid colored curves represent the measured response resulting from the integration over 0.10 eV around the indicated photon energy. The dashed black curves on top are the results of the global fit analysis. The curves have been vertically shifted from each other for clarity.

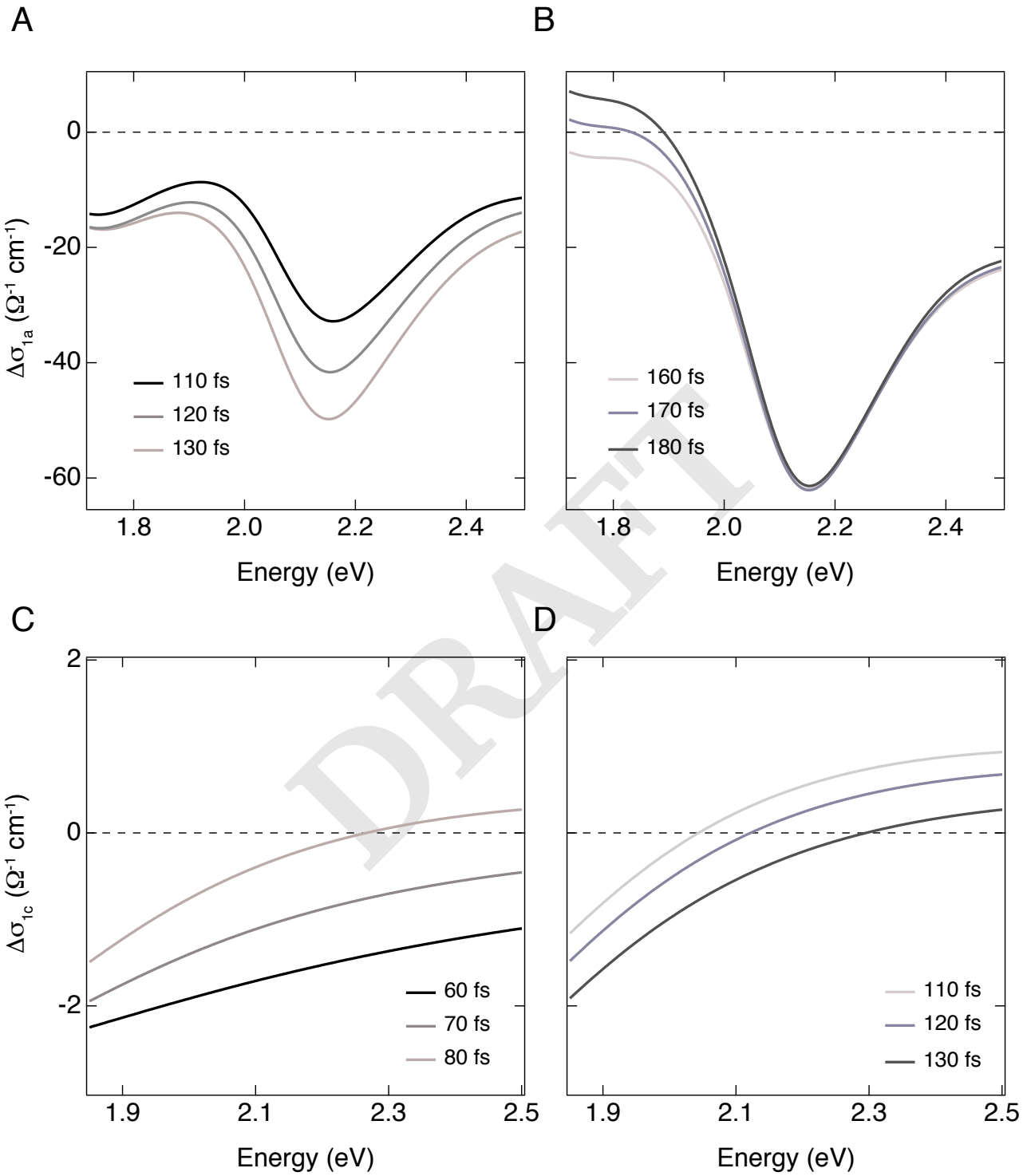

Fig. S10. Temporal evolution of the real part of the optical conductivity ($\Delta\sigma_1$) at different pump-probe time delays. The time delays are selected to highlight similarities between the two responses. *(A,B)* In-plane response during the rise of the signal: (A) 110-130 fs; (B) 160–180 fs. *(C,D)* Out-of-plane response during the rise of the signal: (C) 60-80 fs; (D) 110-130 fs.

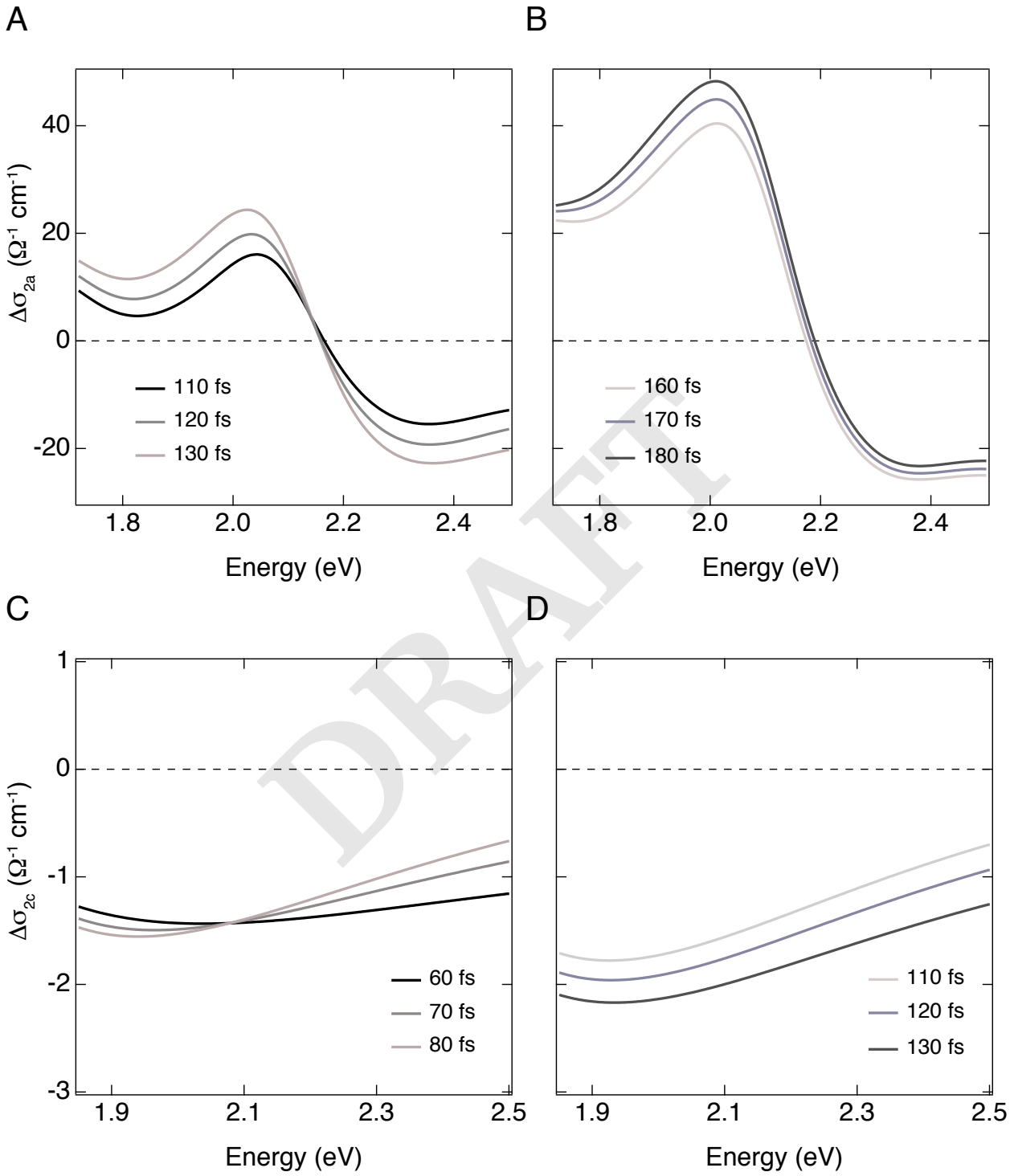

Fig. S11. Temporal evolution of the imaginary part of the optical conductivity ($\Delta\sigma_2$) at different pump-probe time delays. The time delays are selected to highlight similarities between the two responses. *(A,B)* In-plane response during the rise of the signal: (A) 110-130 fs; (B) 160–180 fs. *(C,D)* Out-of-plane response during the rise of the signal: (C) 60-80 fs; (D) 110-130 fs.

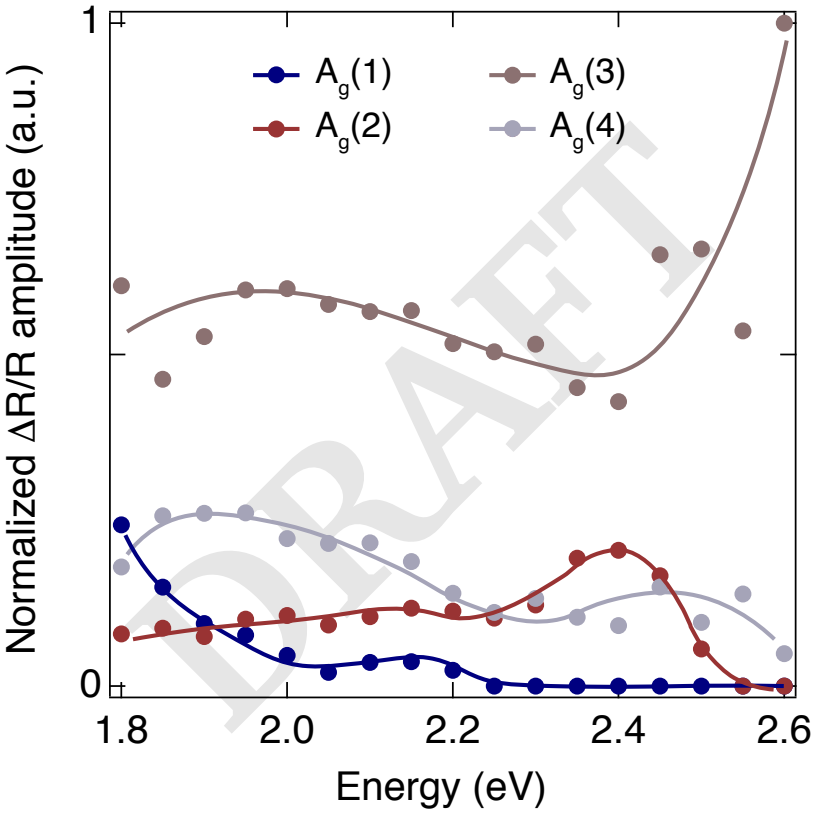

Fig. S12. Normalized ΔR/R oscillation amplitude of four distinct A_g Raman-active modes as a function of photon energy when the pump polarization is set along the a-axis and the probe polarization along the c-axis. Solid lines are used as guides to the eye, *a.u.* refers to arbitrary units.

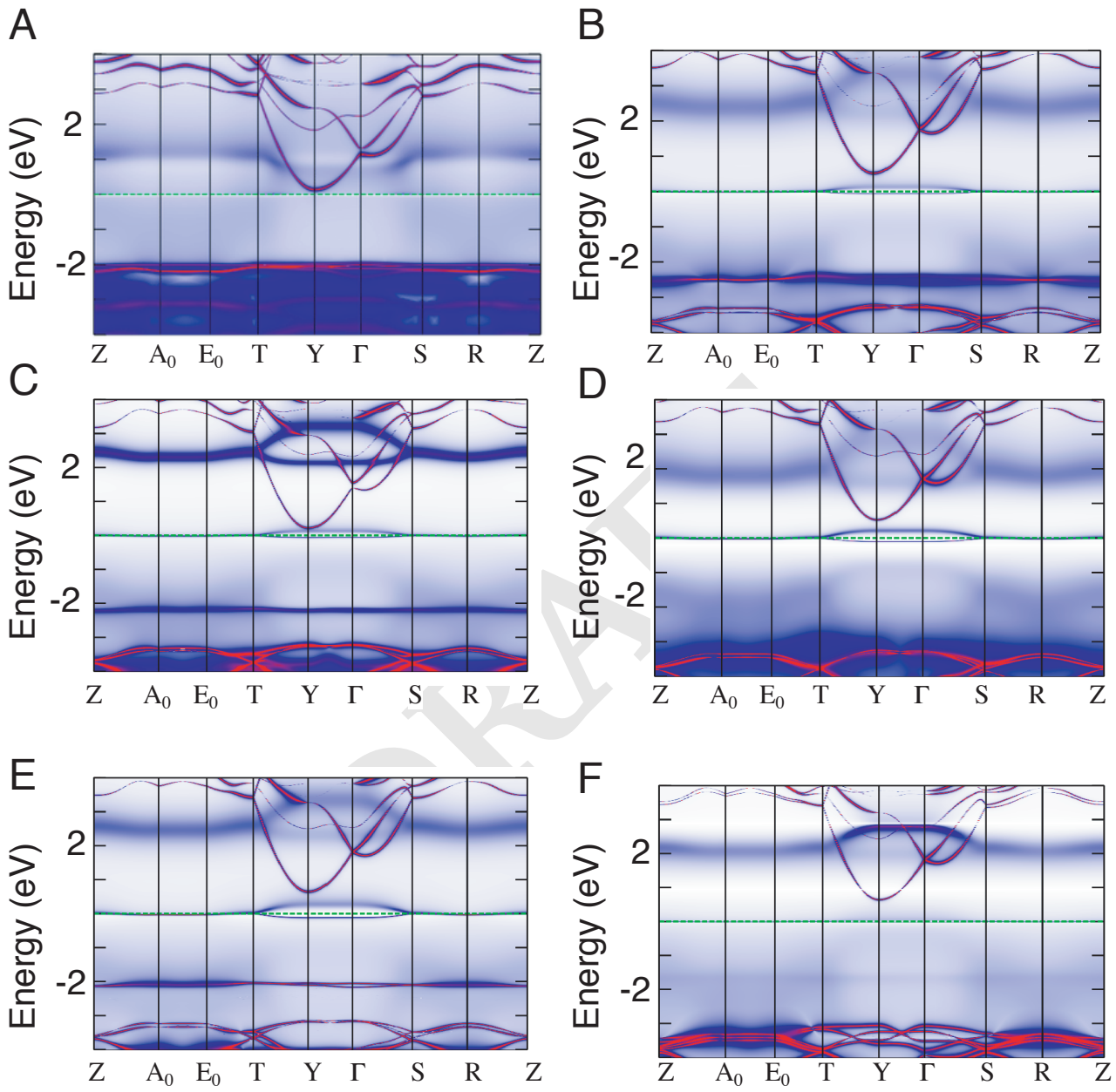

Fig. S13. Electronic spectral function $A(k,\omega)$ of the displaced compound obtained in QSGW+DMFT and resolved in momentum along a path in the Brillouin zone connecting the high-symmetry points. The spectral function is obtained for the structures distorted along the eigenvectors of the A_g and B_g phonon modes calculated by density-functional theory. In particular, the displacements are along *(A)*, the $A_g(1)$ mode, *(B)*, the $A_g(2)$ mode, *(C)*, the $A_g(3)$ mode, *(D)*, the $A_g(4)$ mode, *(E)*, the $A_g(5)$ mode, and *(F)*, the B_{3g} mode coordinates. The electronic structure in the case of all A_g modes exhibits a broad, incoherent 3-peak correlated metallic spectral function, whereas the electronic structure in the case of the B_g modes is gapped. The metallicity in the $A_g(1)$-displaced structure is carried by the incoherent spectral weight crossing the Fermi level, putting this displaced structure on the verge of an IMT. In the three other displaced structures, we observe the formation of a weakly-coherent quasiparticle feature around Fermi energy, along with atomic-like Hubbard band features at high energy. The unoccupied coherent band at Y, near the Fermi level, is the La-d orbital band.

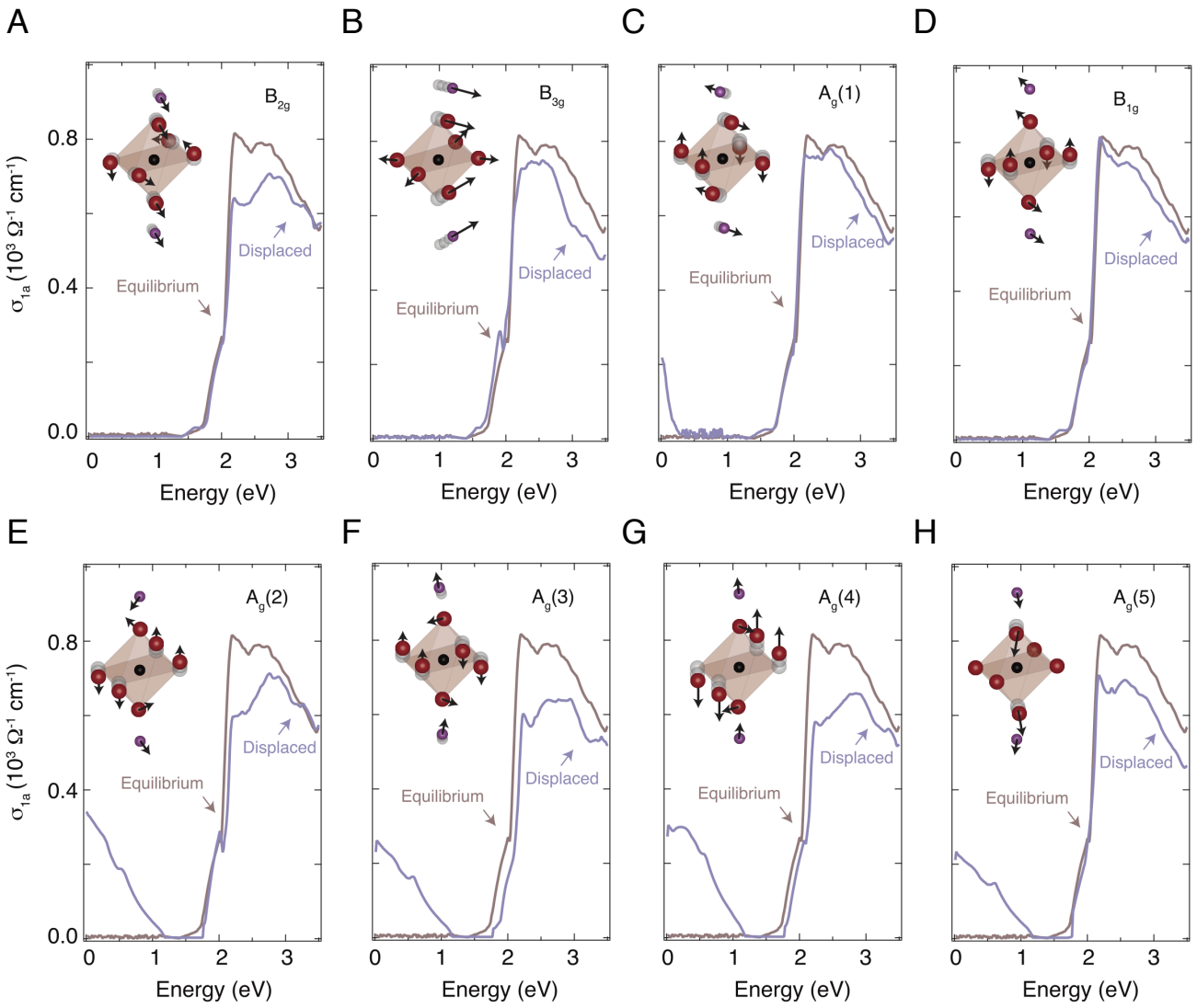

Fig. S14. Theory data from QSGW+DMFT simulations of in-plane optical conductivity for the LCO unit cell displaced by 0.04 Å along different phonon coordinates (indicated in each panel). For displacements along totally-symmetric A_g modes, metallization occurs with spectral weight appearing at low energy below ∼1.00 eV. In contrast, for displacements along B_g modes, there is no metallization and hardly any impact on the low-energy spectral weight inside the optical CT gap. The total spectral weight is conserved over all energies. For the B_g modes, we find that the missing spectral weight from the optical CT build up shifts towards higher energies.

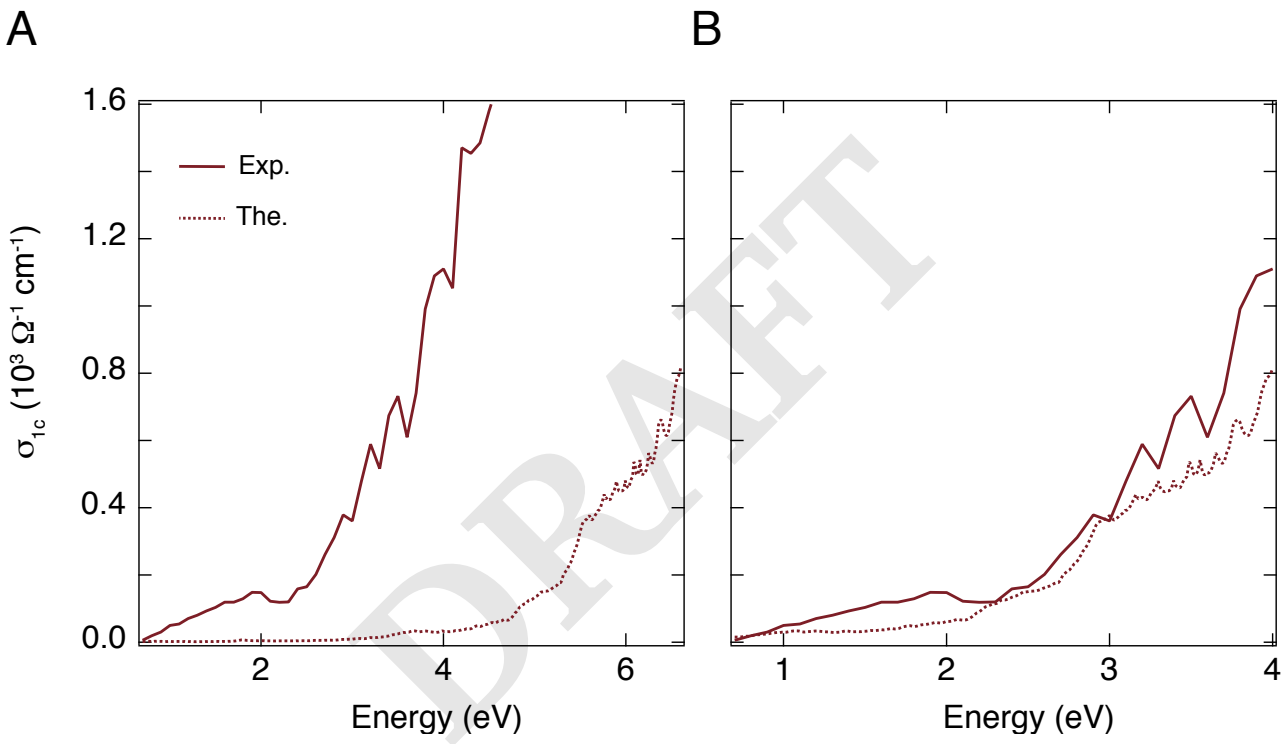

Fig. S15. Real part of the optical conductivity at 10 K, measured with the electric field polarized along the c-axis (brown solid curve). The QSGW+DMFT simulations for the out-of-plane response are shown as a brown dashed curve. (*A*) Comparison between the experimental data and the as-calculated spectrum. The theoretical response is blueshifted with respect to the experimental data due to the lack of electron-hole screening vertex corrections. (*B*) Same data as panel A, but with the theoretical data rigidly redshifted by 2.6 eV. Applying a rigid shift allows to capture the experimental response. We expect the future inclusion of electron-hole scattering vertex correction to provide a contribution similar to this rigid shift. Exp. and The. in the label refer to the experimental and theoretical results.

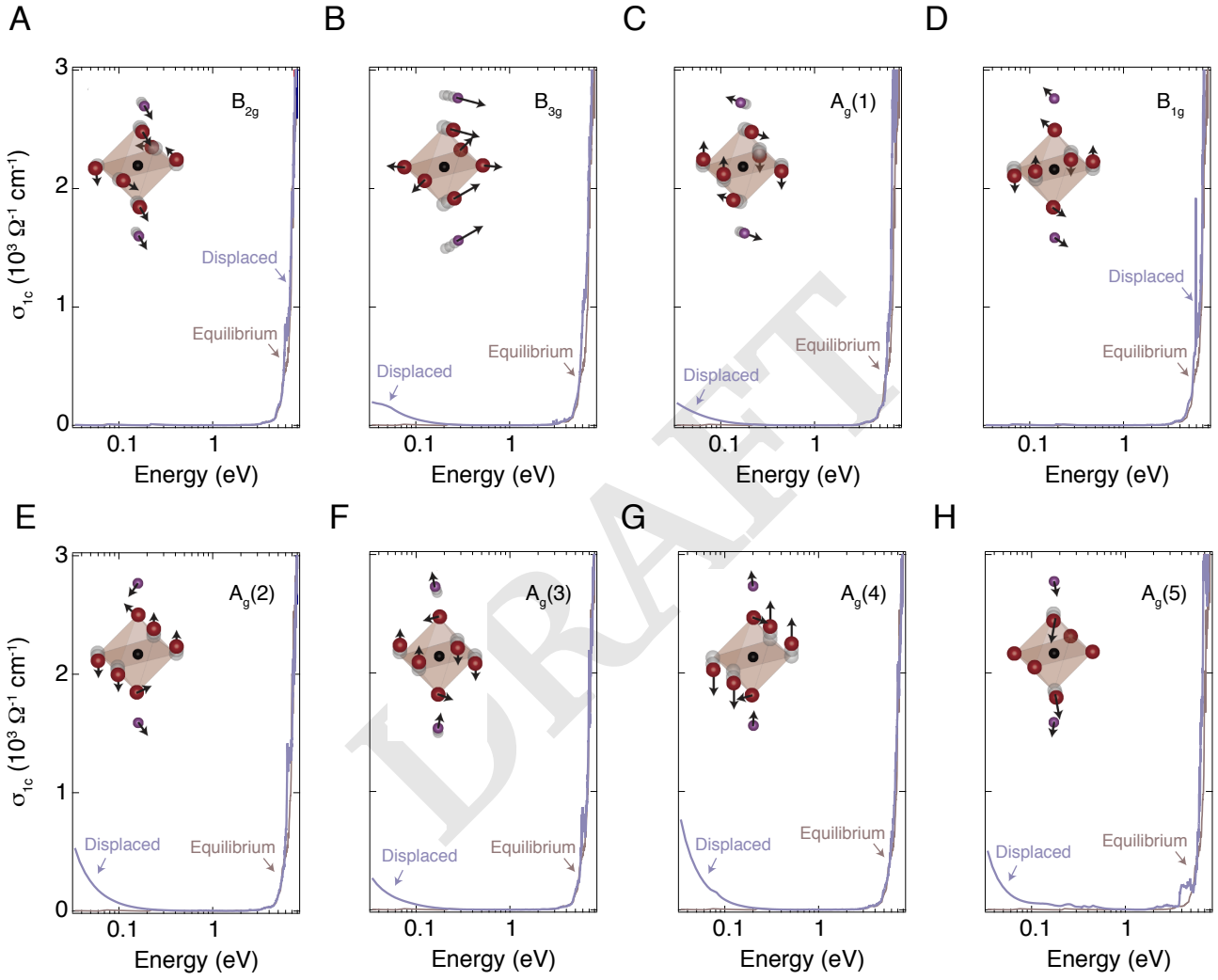

Fig. S16. Theory data from QSGW+DMFT simulations of out-of-plane optical conductivity for the LCO unit cell displaced by 0.04 Å along different phonon coordinates (indicated in each panel). For displacements along totally-symmetric A_g modes, metallization occurs with spectral weight appearing at low energy below ∼1.00 eV. In contrast, for displacements along B_{1g} and B_{2g} modes, there is no metallization and hardly any impact on the low-energy spectral weight inside the optical CT gap. Finally, displacements along the B_{3g} mode coordinates produces incoherent metallization. The total spectral weight is conserved over all energies. To reveal all the features in the spectrum, a logarithmic scale has been used for the energy axis.

1. Jellison Jr GE, et al. (2000) Characterization of thin-film amorphous semiconductors using spectroscopic ellipsometry. *Thin Solid Films* 377:68–73.
2. Falck JP, Levy A, Kastner MA, Birgeneau RJ (1992) Charge-transfer spectrum and its temperature dependence in La_2CuO_4. *Phys. Rev. Lett.* 69(7):1109.
3. McBride JR, Miller LR, Weber WH (1994) Ellipsometric study of the charge-transfer excitation in single-crystal La_2CuO_4. *Phys. Rev. B* 49(17):12224.
4. Ellis DS, et al. (2008) Charge-transfer exciton in La_2CuO_4 probed with resonant inelastic x-ray scattering. *Phys. Rev. B* 77(6):060501.
5. Jorge GA, et al. (2004) Thermodynamic properties of excess-oxygen-doped $La_2CuO_{4.11}$ near a simultaneous transition to superconductivity and long-range magnetic order. *Phys. Rev. B* 69(17):174506.
6. Okamoto H, et al. (2011) Photoinduced transition from Mott insulator to metal in the undoped cuprates Nd_2CuO_4 and La_2CuO_4. *Phys. Rev. B* 83(12):125102.
7. Novelli F, et al. (2014) Witnessing the formation and relaxation of dressed quasi-particles in a strongly correlated electron system. *Nat. Commun.* 5:5112.
8. Mann A, et al. (2015) Probing the electron–phonon interaction in correlated systems with coherent lattice fluctuation spectroscopy. *Phys. Rev. B* 92(3):035147.
9. Mann A, et al. (2016) Probing the coupling between a doublon excitation and the charge-density wave in TaS_2 by ultrafast optical spectroscopy. *Phys. Rev. B* 94(11):115122.
10. Baldini E, et al. (2017) Clocking the onset of bilayer coherence in a high-T_C cuprate. *Phys. Rev. B* 95(2):024501.
11. Borroni S, et al. (2017) Coherent generation of symmetry-forbidden phonons by light-induced electron–phonon interactions in magnetite. *Phys. Rev. B* 96(10):104308.
12. Baldini E, et al. (2018) Lattice-mediated magnetic order melting in $TbMnO_3$. *Phys. Rev. B* 97(12):125149.
13. Baldini E, et al. (2017) Real-time observation of phonon-mediated σ-π interband scattering in MgB_2. *Phys. Rev. Lett.* 119(9):097002.
14. Palmieri T, et al. (2020) Mahan excitons in room-temperature methylammonium lead bromide perovskites. *Nat. Commun.* 11:850.
15. Mansart B, et al. (2012) Evidence for a Peierls phase-transition in a three-dimensional multiple charge-density waves solid. *Proc. Natl. Acad. Sci.* 109(15):5603–5608.
16. Novelli F, et al. (2012) Ultrafast optical spectroscopy of the lowest energy excitations in the Mott insulator compound YVO_3: Evidence for Hubbard-type excitons. *Phys. Rev. B* 86(16):165135.
17. Uchida S, et al. (1991) Optical spectra of $La_{2-x}Sr_xCuO_4$: Effect of carrier doping on the electronic structure of the CuO_2 plane. *Phys. Rev. B* 43(10):7942.
18. Lorenzana J, et al. (2013) Investigating pairing interactions with coherent charge fluctuation spectroscopy. *Eur. Phys. J. Special Topics* 222(5):1223–1239.
19. Uchida S, Tamasaku K, Tajima S (1996) c-axis optical spectra and charge dynamics in $La_{2-x}Sr_xCuO_4$. *Phys. Rev. B* 53(21):14558.
20. Mansart B, et al. (2013) Coupling of a high-energy excitation to superconducting quasiparticles in a cuprate from coherent charge fluctuation spectroscopy. *Proc. Natl. Acad. Sci.* 110(12):4539–4544.
21. Acharya S, et al. (2018) Metal-insulator transition in copper oxides induced by apex displacements. *Phys. Rev. X* 8(2):021038.
22. Nücker N, et al. (1987) Experimental electronic structure studies of $La_{2-x}Sr_xCuO_4$. *Zeit. Phys. B Cond. Matt.* 67(1):9–14.